

Anion-Exchange-Mediated Internal Electric Field: Boosting Photogenerated Carrier Separation and Utilization

Yadong Li (✉ ydli@mail.tsinghua.edu.cn)

Tsinghua University <https://orcid.org/0000-0003-1544-1127>

Tong Han

Tsinghua University

Xing Cao

Tsinghua University

Kaian Sun

China University of Petroleum, Beijing

Qing Peng

Tsinghua University

Weng-Chon Cheong

University of Macau <https://orcid.org/0000-0002-7684-2808>

Zheng Chen

Anhui Normal University <https://orcid.org/0000-0002-4347-0235>

Rui Lin

Ludwig-Maximilians-Universität München

Di Zhao

Beijing Institute of Technology

Zewen Zhuang

Tsinghua University <https://orcid.org/0000-0002-7060-426X>

Chen Chen

Tsinghua University

Dingsheng Wang

Tsinghua University <https://orcid.org/0000-0003-0074-7633>

Article

Keywords: Nanorods, Bulk Anion Layers, Valence Election Localization, Semiconductor Photocatalysts

Posted Date: October 15th, 2020

DOI: <https://doi.org/10.21203/rs.3.rs-88537/v1>

License:  This work is licensed under a Creative Commons Attribution 4.0 International License.

[Read Full License](#)

Version of Record: A version of this preprint was published at Nature Communications on August 16th, 2021. See the published version at <https://doi.org/10.1038/s41467-021-25261-8>.

Abstract

Constructing heterojunctions is a commonly used method for heterogeneous photocatalysts to modulate the internal electric field (IEF); however, this method suffers from narrow IEF distribution (primarily limited at the heterojunction interface) and long migration paths of photocarriers, and therefore results in suboptimal efficiencies in carrier separation and utilization. In this work, we report for the first time novel basic bismuth nitrate compound nanorods (denoted as BOH NRs) featuring surface-exposed open channels and a simple chemical composition; by simply modifying the bulk anion layers to overcome the limitations of heterojunctions, the bulk IEF could be readily modulated. A low exchange ratio ($\sim 10\%$) with halide anions (I^- , Br^- , Cl^-) would give rise to a prominent elevation in carrier separation efficiency; for the reaction of photocatalytic oxidative coupling of benzylamine, the conversions over the modified catalysts are 1.6–2 times as high as that over pristine BOH. Benefiting from the unique crystal structure and the localization of valence electrons, the IEF intensity increases with the atomic number of introduced halide anions, leading to an enhanced efficiency of carrier separation and utilization. Our work here offers new insights into the design and optimization of semiconductor photocatalysts.

Main Text

In recent years, light-powered catalytic organic synthesis has garnered increasing research interests. During photocatalysis, the separation of electron–hole pairs within the semiconductor catalysts, combined with the following energy transfer processes, can readily generate a large amount of highly active species (such as radicals and singlet oxygen^{1–4}). Notably, these active species could, under green and mild conditions, participate in a variety of organic reactions, including hydrogenation^{5,6}, epoxidation^{7,8}, alcohol oxidation^{9,10}, selective oxidation of aromatic compounds^{11,12}, and even some reactions that are rather challenging in thermal catalysis. Yet still, currently for heterogeneous photocatalysts, there exist the common issues of rapid recombination of photocarriers and the resulting low efficiency of carrier separation and utilization, which would hamper the high-performance catalysis of sophisticated organic reactions, and thus their applications have so far been limited primarily to environment-related aspects such as degradation of organics, air purification and water photolysis^{13–17}. A strategy extensively adopted to boost the carrier separation efficiency is to construct composite materials featuring heterojunctions, in which the internal electric field (IEF), resulting from the different band structures at the interface, is expected to facilitate the carrier separation and migration^{18,19}.

However, owing to the poor lattice match at the interface and the resulting structural defects, the composite materials generally suffer from low structural stability and constrained migration of photocarriers; moreover, the IEF thus generated locates merely at the interface, with a rather limited distribution, and therefore is not likely competent to solve the challenging problem of bulk carrier separation^{20–24}. It can thus be envisioned that, if we could somehow synthetically modify the structure of photocatalysts to build a more intense IEF within the entire materials (rather than merely at the heterojunction interfaces) while preserving the original high crystallinity, and to accelerate the carrier

migration to substrate molecules, the resulting photocatalysts would feature a high efficiency of spatial separation of carriers, as well as a high utilization of photogenerated charges²⁵⁻²⁷.

Following the above discussion, in this work we designed and prepared Sillenite-structured single-crystalline basic bismuth nitrate compound nanorods (denoted as BOH NRs) with high aspect ratios (1–6 μm in length, 10–30 nm in diameter). Each NR is composed of multiple (10–30) alternating layers of $[\text{Bi}_2\text{O}_2]^{2+}$ cations and OH^- counteranions stacked along a specific crystallographic direction perpendicular to the longitudinal axis (Scheme 1). Benefiting from this unique structure, the nanorods feature open channels exposed at the surface, and internal electric fields between the alternating layers. Upon light illumination, the generated carriers would be readily separated and transported to the surface along the direction perpendicular to the longitudinal axis of the nanorods, which not only achieves the carrier separation in the bulk phase, but also significantly shortens the migration paths for carriers, and thus effectively promote the utilization of photogenerated electrons and holes. More importantly, this unique structure features an open and ordered arrangement, which enables the modulation of IEF intensity by simply modifying the anion layer; therefore, this catalyst constitutes an ideal model for the theoretical and experimental studies on the relationship between the compositions, structures, and IEF of photocatalysts and their catalytic performances. In our assessment on the reaction of photocatalytic oxidative coupling of benzylamine, we found that, with a low ratio ($\sim 10\%$) of halide anions (I^- , Br^- , Cl^-) introduced to substitute OH^- in the catalyst, the conversions of benzylamine became 1.6–2 times as high as that over the unmodified BOH, indicating an enhanced efficiency of carrier separation and utilization.

Density functional theory (DFT) calculations reveal that, after halide exchange, the bulk IEF within the BOH NRs become significantly intensified; the IEF intensity increases with the atomic number of halide anions, and a similar trend was found for the benzylamine conversion over different halide-exchanged catalysts. Such a difference in the efficiency of carrier separation and utilization results simply from the different halide anions introduced, and could be attributed primarily to the variation in electrostatic potential difference between neighboring layers (i.e., the IEF), which is sensitive to the localization of valence electrons and the interlayer spacing. Our study here not only develops a high-performance photocatalyst featuring bulk-IEF-facilitated charge separation, but also clearly demonstrates the effectiveness of boosting IEF intensity and photocatalytic performances via ion exchange, and therefore offers new insights for exploring advanced photocatalysts and high-performance photocatalytic organic reactions.

Results

Synthesis strategy and characterization of BOH nanorods. The Sillenite-structured BOH NRs were prepared by a hydrothermal method, with surfactants added to regulate the hydrolysis of $\text{Bi}(\text{NO}_3)_3$ precursor. Specifically, $\text{Bi}(\text{NO}_3)_3 \cdot 5\text{H}_2\text{O}$, PVP (polyvinyl pyrrolidone-8K) and mannitol were dissolved in deionized water under stirring, and the resulting mixture was subjected to hydrothermal treatment at 160 $^\circ\text{C}$ for 24 h. As shown in the scanning electron microscopy (SEM) and transmission electron

microscopy (TEM) images (Fig. 1a and the inset), the product BOH has a morphology of NRs with high aspect ratios (10–30 nm in diameter, 1–6 μm in length); most NRs aggregate into bundles by connecting at the middle or one end. The introduction of PVP and mannitol proved critical for the formation of NRs: as shown in Fig. S1 (in Supporting Information), without mannitol, the product has a rod-like morphology, but the NRs are shorter in length and not uniform in diameter; without PVP, the product has a sheet-like morphology. These results indicate that PVP can regulate the growth of BOH along specific directions, thus exposing specific facets and leading to the formation of NRs; mannitol can promote the dissolution of $\text{Bi}(\text{NO}_3)_3 \cdot 5\text{H}_2\text{O}$ in water, leading to uniform nucleation of BOH and the resulting NRs with high uniformity and aspect ratios²⁸.

The high-angle annular dark-field scanning transmission electron microscopy (HAADF-STEM) image and the energy-dispersive X-ray (EDX) mapping results (Fig. 1b–d) confirm that in the BOH NRs, the Bi and O elements are evenly distributed. The selected-area electron diffraction (SAED) pattern (Fig. 1e) and high-resolution TEM (HRTEM) image (Fig. 1f) reveal that each BOH NR is of single crystallinity and has well-ordered lattice fringes. The hydrolysis of $\text{Bi}(\text{NO}_3)_3 \cdot 5\text{H}_2\text{O}$ can yield multiple products including $\text{Bi}_5\text{O}_7(\text{NO}_3)$ or basic bismuth nitrates ($\text{Bi}_6\text{O}_6(\text{OH})_2(\text{NO}_3)_4 \cdot 2\text{H}_2\text{O}$, $\text{Bi}_6\text{O}_5(\text{OH})_3(\text{NO}_3)_5 \cdot 3\text{H}_2\text{O}$, $\text{Bi}_2\text{O}_2(\text{OH})(\text{NO}_3)$ etc.). All of these products are made of backbones of [Bi–O] layers, with anion layers intercalated in between; the main differences are the arrangement of Bi and O atoms in [Bi–O] layers, and the types and amounts of anions (such as NO_3^- and OH^-)^{29–31}. It is such differences that result in the variation in the X-ray diffraction (XRD) patterns of the hydrolysis products of $\text{Bi}(\text{NO}_3)_3$. By comparing with the XRD pattern (Fig. S2) for the hydrothermal product without PVP (denoted as BOH-nPVP), we confirmed that PVP only plays a role of regulating the nucleation and growth of products. For our BOH NRs, the XRD pattern (Fig. 1h) does not match well with any standard XRD pattern available; yet still, considering the common hydrolysis products of $\text{Bi}(\text{NO}_3)_3$, it could be inferred that our BOH has a similar basic structure with alternating [Bi–O] and anion layers. In this regard, we performed aberration-corrected HAADF-STEM (AC HAADF-STEM) with atomic resolution. Fig. S3 shows that the BOH NR is composed of ~ 10 ordered layers arranged in parallel, each layer with a thickness of ~ 1 nm. In Fig. 1g, it can be clearly observed that each layer has two arrays of Bi atoms (Bi atoms appear as bright dots in the image, whereas O atoms are barely observable owing to the small atomic number), and the inter-array spacing is 0.27 nm, which is identical to that within the $[\text{Bi}_2\text{O}_2]^{2+}$ layer of the known compound $\text{Bi}_2\text{O}_2(\text{OH})(\text{NO}_3)$ (that is, the distance between two neighboring red balls in Fig. 1g) (for the XRD patterns of the two compounds, see Fig. S4; for the two-dimensional structure of $\text{Bi}_2\text{O}_2(\text{OH})(\text{NO}_3)$, see Fig. S5). The results above confirm that our BOH NRs have a layered $[\text{Bi}_2\text{O}_2]^{2+}$ structure similar to that in $\text{Bi}_2\text{O}_2(\text{OH})(\text{NO}_3)$, and the interlayer channels are openly exposed. The alternating $[\text{Bi}_2\text{O}_2]^{2+}$ and anion layers are stacked via van der Waals interaction, forming a layered Sillenite structure; between the neighboring $[\text{Bi}_2\text{O}_2]^{2+}$ and anion layers exists a perpendicular IEF, which could facilitate the carrier separation^{32,33}. In addition, the IEF is also perpendicular to the normal of the exposed facets of BOH, and thus shortens the migration path for photocarriers, which is conducive to the transport and separation of charges³⁴.

In order to probe the chemical identity of the intercalating anions, we performed X-ray photoelectron spectroscopy on the $\text{Bi}(\text{NO}_3)_3 \cdot 5\text{H}_2\text{O}$ precursor, the PVP surfactant and the product BOH NRs. The N 1s spectra (Fig. 1i) show that the binding energies of N (399.3 eV and 406.5 eV) in the BOH sample are similar to those for PVP, and different with that for NO_3^- (407.1 eV). These results indicate that there barely exists any NO_3^- within the 10 nm subsurface region (which constitutes almost the entire volume) of the BOH NR. Figure 1j shows the O 1s peaks at 529.0 eV, 530.5 eV and 531.9 eV for BOH, corresponding to the binding energies of O atoms in Bi–O bonds in the $[\text{Bi}_2\text{O}_2]^{2+}$ layer, the C = O groups in PVP, and OH^- anions, respectively. These results also explain our finding that the XRD patterns for BOH and $\text{Bi}_2\text{O}_2(\text{OH})(\text{NO}_3)$ do not ideally match: NO_3^- anion has a larger radius (2.00 Å) than OH^- (0.89 Å), so when OH^- anions are intercalated between the $[\text{Bi}_2\text{O}_2]^{2+}$ layers (in the case of BOH) instead of NO_3^- (in the case of $\text{Bi}_2\text{O}_2(\text{OH})(\text{NO}_3)$), the bridging effect of the anions would become less pronounced, leading to an increased spacing between neighboring $[\text{Bi}_2\text{O}_2]^{2+}$ layers owing to coulombic repulsion³⁵. This is in good consistency with the fact that the first primary XRD peak for BOH ($2\theta = 7.7^\circ$) shifts to lower angles; the altered symmetry for BOH also results in diffraction peaks located at different angles from those for $\text{Bi}_2\text{O}_2(\text{OH})(\text{NO}_3)$, as well as more diffraction peaks. Therefore, we infer that the BOH NRs have a backbone structure similar to that for $\text{Bi}_2\text{O}_2(\text{OH})(\text{NO}_3)$, only with OH^- anions intercalated between the $[\text{Bi}_2\text{O}_2]^{2+}$ layers.

Owing to the alternating arrangement of $[\text{Bi}_2\text{O}_2]^{2+}$ and anion layers, the hydrolysis products of $\text{Bi}(\text{NO}_3)_3 \cdot 5\text{H}_2\text{O}$ are usually $\text{Bi}_5\text{O}_7(\text{NO}_3)$ or basic bismuth nitrates with sheet-like morphologies; yet in this work, by introducing PVP and mannitol during the hydrolysis, we obtained rod-like structures with barely any NO_3^- and with interlayer channels openly exposed. Compared with conventional sheet-like products, this rod-like structure can shorten the paths for photocarriers to migrate from the interior to the surface, and the holes accumulated at the surface-exposed anion layers can be utilized to activate substrate molecules. In addition, by taking advantage of the openly exposed channels, the anion layers may be modified in both composition and structure.

Synthesis strategy and characterization of BOX nanorods (X = Cl, Br, I). We used the BOH NRs as precursors for subsequent anion exchange experiments. Specifically, BOH NRs were dispersed in deionized water, and a proper amount of KX (X = Cl, Br, I) was added. The mixture was sonicated, sealed in an autoclave and then heated at 60 °C for 12 h. As shown in Fig. 2a, during the reaction process, the OH^- anions between the $[\text{Bi}_2\text{O}_2]^{2+}$ layers could partially exchange with halide anions, and the resulting products could well preserve the rod-like morphology and the backbone structure of unmodified BOH NRs. The products after exchange with KI, KBr and KCl are hereafter denoted as BOH-I, BOH-Br and BOH-Cl, respectively (and collectively as BOH-X).

Similar to the pristine BOH NRs, all three BOH-X samples have a rod-like morphology with diameters of 10–30 nm and lengths of 1–6 μm (Fig. 2b–d and Fig. S6). EDX mapping (Fig. 2e–g and Fig. S7–9) showed uniform distributions of halogen atoms over the NRs after anion exchange; HRTEM-STEM

images and the corresponding SAED patterns (Fig. 2h–j) revealed well-preserved single crystallinity for the BOH-X NRs. The XRD patterns for the three BOH-X samples (Fig. S10) are almost identical; yet the primary peaks (at $2\theta = 7.7^\circ$ for BOH) shift toward lower angles to different extents, indicating that the intercalation of halide anions has altered the interlayer spacings. In addition, the XPS spectra (Fig. S11a) revealed that the binding energies of Bi 4f in the BOH-X samples were elevated by less than 1 eV with respect to that for BOH, confirming that the highly electronegative halide anions had been introduced successfully. By comparing peak areas of the Bi–O bond and O–H bond in the XPS spectra (Fig. S12), we found that the ratios of the O–H bond became lower for BOH-X, again confirming the success of halide exchange and intercalation. Semi-quantitative analyses based on the XPS data revealed that after anion exchange, the X^-/Bi^{3+} ratios are 0.12 (for I), 0.09 (for Br), and 0.11 (for Cl), indicating similar activities of ion exchange for the halide anions. To unveil the distribution of halogen atoms, we selected BOH-I as a representative and performed High-resolution XPS experiments with Ar^+ sputtering at different depths (Fig. 3 and Fig. S13). As the sputtering depth (14 nm) is nearly equal to (or larger than) the radii of the NRs, the results suggest that I^- anions are evenly distributed within the entire volume, rather than merely at the surface. In addition, no prominent peaks corresponding to N were observed at the subsurface region, again implying that the N atoms come of PVP, and are distributed primarily at the surface. All the above results confirmed the efficacy of modifying the bulk anion layers of BOH via hydrothermal halide-anion exchange.

Spectroscopic characterization of BOH and BOX nanorods. The photoluminescence (PL) spectra (Fig. 4a) of BOH and BOH-X samples show that all four samples give an emission peak at 552 nm. The PL intensities for the BOH-X are all lower than that for BOH, and the intensity decreases with the atomic number of halide anions. The decrease in PL intensity indicates suppression on the recombination of photocarriers, which we believe can be explained as follows: after X^- exchange to replace OH^- , the charge distribution at the anion layers becomes more uneven, leading to strengthen the internal electric field resulting from the polarization of atoms and orbitals in vicinity²¹. The results of transient PL spectroscopy (Fig. 4b and Table S1) further validated our inference above. The average luminescence lifetimes are 3.68 ns for BOH, 3.17 ns for BOH-Cl, 2.63 ns for BOH-Br and 1.96 ns for BOH-I. A shorter PL lifetime indicates that the photo-excitons are more prone to separate rather than to recombine^{36–39}.

The introduction of halide anions may modify the band structure of the photocatalyst. As shown in the UV–vis diffuse reflectance spectra (DRS) (Fig. 4c), the exchange with Cl^- and Br^- did not affect the absorption edge for the pristine BOH (359 nm), so BOH, BOH-Cl and BOH-Br have similar light absorption ranges and similar bandgaps (3.45 eV). By contrast, the exchange with I^- induced a redshift of the absorption edge from 359 nm to 420 nm, indicating a narrower bandgap for BOH-I (2.95 eV), and an enhanced absorption in the visible region.

The positive slopes in the Mott–Schottky plots (Fig. S14) revealed a character of n-type semiconductor for all four samples, and a flat band potential ranging within $-0.55 \sim -0.34$ eV. As the conduction band position is near the flat band potential for n-type semiconductor⁴⁰, BOH-I has the lowest CBM, and the

CBM for BOH, BOH-Cl, BOH-Br are higher by 0.13 eV, 0.19 eV, 0.21 eV, respectively. In combination with the UV-vis DRS results, now we can draw the diagrams of the band structures of the four samples (Fig. 4d). Compared with pristine BOH, all BOH-X samples have higher valence band maxima (VBM), and BOH-I has the highest VBM; yet the alterations in VBM are not quite significant. To sum up, the anion exchange induces a moderate change in light absorption only for BOH-I, whereas its influences on the band structures of BOH-X are rather limited.

Photocatalytic performances. Imide derivatives are of major importance for the industries of fine chemicals and pharmaceuticals⁴¹⁻⁴³. We selected the reaction of visible-light-driven photocatalytic oxidative coupling of benzylamine (Fig. 5a) as the model reaction to assess the effect on catalytic performances induced by halide exchange. Fig. 5b shows that with a low ratio (~10%, as mentioned above) of OH⁻ in pristine BOH replaced by Cl⁻, Br⁻ and I⁻, the conversion of benzylamine was elevated from 44.1% up to 71.0%, 78.3% and 88.3%, respectively, and the selectivity was between 96.3% and 99.0%. The samples of BOH, BOH-Br and BOH-Cl have almost identical absorption edges, yet their catalytic performances are rather different, indicating that in this case the band structure is not a key influencing factor for the catalytic performance. Since the conversion of benzylamine and the efficiency of carrier separation both follow the same order (BOH < BOH-Cl < BOH-Br < BOH-I), we speculate that the difference in carrier separation and utilization may be attributed to the variation in IEF. As the atomic number of the introduced halide species goes higher, the ionic radius becomes larger, and the charge distribution between the layers become more uneven; the larger electrostatic potential difference between the layers intensifies the interlayer IEF, and thus promotes the carrier separation and utilization. In addition, we also tested the BOH-nPVP nanosheets (that is, the hydrothermal product obtained without PVP) under identical catalytic conditions (Fig. S15), and the sample gave a benzylamine conversion of only 6.5%, far lower than that of BOH. This result indicates that the NRs have a superior photocatalytic activity than the nanosheets, probably because the high aspect ratio of the NRs is conducive to the migration and separation of charge carriers. Subsequently, we assessed the durability of the champion sample BOH-I; after five cycles, the benzylamine conversion was well retained at 77.9%, with selectivity of 98.8% (Fig. 5c). The morphology and microstructure of the catalyst recycled after five runs were also well preserved (as shown in Fig. S16).

Photocatalytic mechanism. We carried out a series of comparative experiments as well as quenching experiments on the possible active species (Fig. 5d). For example, in the case of BOH-I, the conversion of benzylamine is rather low in dark or without the photocatalyst, indicating that both the catalyst and light are essential for this reaction. The conversion in Ar atmosphere was also only marginal, manifesting the essentialness of oxygen. The semiconductor photocatalysts utilize photogenerated electrons and holes to participate in the reaction; the holes can directly oxidize the substrate molecules, and the electrons may reduce molecular oxygen into superoxide radical (\check{O}_2^-) to oxidize the substrate. In order to unveil the reaction mechanism, we added K₂S₂O₈ or triethanolamine (TEOA) as the scavenging agent for electrons or holes, respectively. The results show that with either agent introduced, the catalytic performances over all four samples declined. Compared with K₂S₂O₈, TEOA would lead to a much more pronounced decline

in conversion, particularly for the halide-modified catalysts. These results suggest that both the electrons and holes function as the active species to participate in the catalytic conversion, the latter playing a major role; moreover, after halide-anion exchange, the role of holes (which were mainly collected in anionic layers) becomes even more pronounced. To investigate the influence of $\check{z}O_2^-$ on the reaction pathways, we conducted comparative experiments on radical quenching (Fig. S17). After the introduction of SOD (superoxide dismutase), the selectivity over BOH-I showed a minor decline, from 88.3–74.1%. In addition, the electron paramagnetic resonance (EPR) data on $\check{z}O_2^-$ (Fig. S18) also revealed that, the halide-modified samples are more active in activating O_2 into $\check{z}O_2^-$ under visible light; the three BOH-X samples give $\check{z}O_2^-$ signals of similar intensity, implying that $\check{z}O_2^-$ is not responsible for the difference in their catalytic activities. To sum up, it can be concluded that the photogenerated holes are the major active species for oxidizing the substrate molecules, and the promotion in catalytic performances after halide exchange is due to the enhanced IEF and in turn the elevated efficiency of carrier separation.

Theoretical insights on the modulating effect of halide anions. Three bulk BOH-X models were adopted (Fig. 6a–d), with the (001), (100) and (010) facets highlighted for surface cleavage. Owing to the different atomic radii of halides (0.97 Å for Cl, 1.12 Å for Br, 1.32 Å for I), the interlayer spacings of BOH-X are altered (13.6 Å for BOH-Cl, 13.7 Å for BOH-Br, and 13.8 Å for BOH-I), which is in good consistency with the XRD results above.

Furthermore, the calculated DOS (Density of State) confirmed that halide anions in the (001) facet would induce an altered the local electronic structure. Compared with Cl^- and Br^- , the introduction of I^- would greatly promote the uneven charge distribution in the cation and anion layers. As shown in the calculated DOS (Fig. 6e and Fig. S19–22), the p orbital of the introduced halide anion hybridized with the p states of both Bi and O. The introduction of I^- would lead to a more pronounced alteration in the bandgap, in contrast to the cases for Br^- and Cl^- , which is in good accordance with the UV–vis DRS data. However, as the energy levels of valence-shell orbitals are different for holes, as well as the utilization of holes². The localization of valence electrons and the altered interlayer spacing collectively induce a change in the IEF between the cation and anion layers. Our calculations revealed that the electrostatic potential differences in the halide-modified samples are 0.47 eV (for BOH-Cl), 0.49 eV (for BOH-Br) and 0.51 eV (for BOH-I), all higher than the 0.42 eV for pristine BOH. This trend is in good accordance with the trend for the catalytic conversion of benzylamine (Fig. 6f–g). As a result, we believe that the elevation in the efficiency of carrier separation and utilization is primarily attributed to the enhanced IEF intensity between the layers.

Conclusions

In conclusion, we report for the first time a novel Sillenite-structured nanorod material, which features alternating layers of $[Bi_2O_2]^{2+}$ and OH^- ions, and open channels exposed at the surface; on the basis of the pristine nanorods, we have developed an effective strategy to controllably regulate the internal electric field within the material by introducing a low ratio of halide anions to replace the OH^- ions therein. The experimental results and theoretical calculations unveiled the mechanism of IEF regulation: as the atomic

number of halide anions goes higher, the spacing between $[\text{Bi}_2\text{O}_2]^{2+}$ layers exchanges, and the localization of valence electrons becomes more pronounced. This facile method, based on halide-anion exchange with Sillenite-structured compounds, represents a breakthrough from conventional methods on tuning the electronic structures of photocatalysts (such as broadening the absorption range, and modulating band alignment), and circumvents the typical issue (for conventional photocatalysts) of resorting to limited “heterojunction interfaces” to separate photocarriers. Therefore, this method can effectively enhance the efficiency of carrier separation and utilization. We believe that our work here offers new insights into the design and optimization of advanced high-performance photocatalysts

Declarations

Acknowledgments

This work was supported by the National Key R&D Program of China (2017YFA0700101, 2016YFA0202801), the National Natural Science Foundation of China (21971135, 21925202, 21872076, 21590792), Beijing Natural Science Foundation (JQ18007). Also, we thank Dr. C. Zhang for the help in preparing this manuscript.

Author Contributions

T. H., X. C., Q. P. and Y. L. conceived the idea. T. H., X. C., W-C. C. carried out the sample synthesis, characterization and electrochemical test. K. S. and C. C. conducted the DFT calculation. T. H, X. C. and Q. P. wrote the manuscript. R. L. Z. Z., and D. W. discussed the electrocatalytic measurements and gave useful suggestions. Z. C. and D. Z. discussed the organic reactions and gave useful suggestions. Q. P., and Y. L. was responsible for the overall direction of the project. All the authors contributed to the overall scientific interpretation and edited the manuscript. T. H., X. C. and K. S. contributed equally to this work.

Author Information

Reprints and permissions information is available at www.nature.com/reprints. The authors declare no competing financial interests. Readers are welcome to comment on the online version of the paper. Correspondence and requests for materials should be addressed to Q. P. (pengqing@mail.tsinghua.edu.cn) and Y. L. (ydli@mail.tsinghua.edu.cn).

References

1. Wang, H. *et al.* Oxygen-vacancy-mediated exciton dissociation in BiOBr for boosting charge-carrier-involved molecular oxygen activation. *J Am Chem Soc* **140**, 1760–1766, doi:10.1021/jacs.7b10997 (2018).

2. Wang, H. *et al.* Giant electron-hole interactions in confined layered structures for molecular oxygen activation. *J Am Chem Soc* **139**, 4737–4742, doi:10.1021/jacs.6b12273 (2017).
3. Schweitzer, C. & Schmidt, R. Physical mechanisms of generation and deactivation of singlet oxygen. *Chemical Reviews* **103**, 1685–1758, doi:10.1021/cr010371d (2003).
4. Nosaka, Y. & Nosaka, A. Y. Generation and detection of reactive oxygen species in photocatalysis. *Chemical Reviews* **117**, 11302–11336, doi:10.1021/acs.chemrev.7b00161 (2017).
5. Yu, Z. J. *et al.* Photocatalytic hydrogenation of nitroarenes using Cu_{1.94}S-Zn_{0.23}Cd_{0.77}S heteronanorods. *Nano Res* **11**, 3730–3738, doi:10.1007/s12274-017-1944-1 (2018).
6. Shen, M. *et al.* Room-temperature chemoselective reduction of 3-Nitrostyrene to 3-Vinylaniline by ammonia borane over Cu nanoparticles. *J Am Chem Soc* **140**, 16460–16463, doi:10.1021/jacs.8b11303 (2018).
7. Zhang, X., Kumari, G., Heo, J. & Jain, P. K. In situ formation of catalytically active graphene in ethylene photo-epoxidation. *Nat Commun* **9**, 3056, doi:10.1038/s41467-018-05352-9 (2018).
8. Kominami, H., Yamamoto, S., Imamura, K., Tanaka, A. & Hashimoto, K. Photocatalytic chemoselective reduction of epoxides to alkenes along with formation of ketones in alcoholic suspensions of silver-loaded titanium(IV) oxide at room temperature without the use of reducing gases. *Chemical Communications* **50**, 4558–4560, doi:10.1039/C3CC49340G (2014).
9. Courtois, C. *et al.* Reactions in the photocatalytic conversion of tertiary alcohols on rutile TiO₂ (110). *Angew Chem Int Ed Engl* **58**, 14255–14259, doi:10.1002/anie.201907917 (2019).
10. Jiang, N. *et al.* (Metal yolk)/(porous ceria shell) nanostructures for high-performance plasmonic photocatalysis under visible light. *Nano Res* **13**, 1354–1362, doi:10.1007/s12274-019-2599-x (2020).
11. Cao, X. *et al.* A photochromic composite with enhanced carrier separation for the photocatalytic activation of benzylic C–H bonds in toluene. *Nature Catalysis* **1**, 704–710, doi:10.1038/s41929-018-0128-z (2018).
12. Sarina, S. *et al.* Driving selective aerobic oxidation of alkyl aromatics by sunlight on alcohol grafted metal hydroxides. *Chemical Science* **3**, 2138–2146, doi:10.1039/C2SC20114C (2012).
13. Anwer, H. *et al.* Photocatalysts for degradation of dyes in industrial effluents: Opportunities and challenges. *Nano Res* **12**, 955–972, doi:10.1007/s12274-019-2287-0 (2019).
14. Xu, T. *et al.* New and stable g-C₃N₄/HAp composites as highly efficient photocatalysts for tetracycline fast degradation. *Applied Catalysis B: Environmental* **245**, 662–671, doi:10.1016/j.apcatb.2019.01.020 (2019).
15. Bertolini, G. R., Pizzio, L. R., Kubacka, A., Muñoz-Batista, M. J. & Fernández-García, M. Composite H₃PW₁₂O₄₀-TiO₂ catalysts for toluene selective photo-oxidation. *Applied Catalysis B: Environmental* **225**, 100–109, doi:10.1016/j.apcatb.2017.11.055 (2018).
16. Tang, Y. *et al.* Face-to-face engineering of ultrathin Pd nanosheets on amorphous carbon nitride for efficient photocatalytic hydrogen production. *Science China Materials* **62**, 351–358, doi:10.1007/s40843-018-9327-y (2019).

17. Ma, B., Zhao, J., Ge, Z., Chen, Y. & Yuan, Z. 5 nm NiCoP nanoparticles coupled with g-C₃N₄ as high-performance photocatalyst for hydrogen evolution. *Science China Materials* **63**, 258–266, doi:10.1007/s40843-019-1181-y (2020).
18. Low, J., Yu, J., Jaroniec, M., Wageh, S. & Al-Ghamdi, A. A. Heterojunction photocatalysts. *Adv Mater* **29**, 1601694, doi:10.1002/adma.201601694 (2017).
19. Bai, S., Gao, C., Low, J. & Xiong, Y. Crystal phase engineering on photocatalytic materials for energy and environmental applications. *Nano Res* **12**, 2031–2054, doi:10.1007/s12274-018-2267-6 (2019).
20. Simon, T., Carlson, M. T., Stolarczyk, J. K. & Feldmann, J. Electron transfer rate vs recombination losses in photocatalytic H₂ generation on Pt-decorated CdS nanorods. *ACS Energy Letters* **1**, 1137–1142, doi:10.1021/acsenergylett.6b00468 (2016).
21. Li, J., Cai, L., Shang, J., Yu, Y. & Zhang, L. Giant enhancement of internal electric field boosting bulk charge separation for photocatalysis. *Adv Mater* **28**, 4059–4064, doi:10.1002/adma.201600301 (2016).
22. Zhu, X. *et al.* Novel high-efficiency visible-light responsive Ag₄(GeO₄) photocatalyst. *Catalysis Science & Technology* **7**, 2318–2324, doi:10.1039/C7CY00393E (2017).
23. Su, Y., Zhang, L. & Wang, W. Internal polar field enhanced H₂ evolution of BiOIO₃ nanoplates. *International Journal of Hydrogen Energy* **41**, 10170–10177, doi:10.1016/j.ijhydene.2016.04.236 (2016).
24. Jiang, L., Zhang, Y., Qiu, Y. & Yi, Z. Improved photocatalytic activity by utilizing the internal electric field of polar semiconductors: a case study of self-assembled NaNbO₃ oriented nanostructures. *RSC Adv.* **4**, 3165–3170, doi:10.1039/c3ra45954c (2014).
25. Guo, Y., Shi, W. & Zhu, Y. Internal electric field engineering for steering photogenerated charge separation and enhancing photoactivity. *EcoMat* **1**, 12007, doi:10.1002/eom2.12007 (2019).
26. Li, M., Huang, H., Yu, S., Tian, N. & Zhang, Y. Facet, junction and electric field engineering of bismuth-based materials for photocatalysis. *ChemCatChem* **10**, 4477–4496, doi:doi:10.1002/cctc.201800859 (2018).
27. Chen, F., Huang, H., Guo, L., Zhang, Y. & Ma, T. The role of polarization in photocatalysis. *Angew Chem Int Ed Engl* **58**, 10061–10073, doi:10.1002/anie.201901361 (2019).
28. Guan, M. *et al.* Vacancy associates promoting solar-driven photocatalytic activity of ultrathin bismuth oxychloride nanosheets. *Journal of the American Chemical Society* **135**, 10411–10417, doi:10.1021/ja402956f (2013).
29. Gong, S., Han, Q., Wang, X. & Zhu, J. Controlled synthesis of bismuth-containing compounds (α-, β- and δ-Bi₂O₃, Bi₅O₇NO₃ and Bi₆O₆(OH)₂(NO₃)₄·2H₂O) and their photocatalytic performance. *CrystEngComm* **17**, 9185–9192, doi:10.1039/c5ce01787d (2015).
30. Pang, J. *et al.* Two basic bismuth nitrates: [Bi₆O₆(OH)₂](NO₃)₄·2H₂O with superior photodegradation activity for rhodamine B and [Bi₆O₅(OH)₃](NO₃)₅·3H₂O with ultrahigh adsorption capacity for methyl orange. *Applied Surface Science* **422**, 283–294, doi:10.1016/j.apsusc.2017.06.022 (2017).

31. Huang, H. W. *et al.* Bi₂O₂(OH)(NO₃) as a desirable [Bi₂O₂]²⁺ layered photocatalyst: strong intrinsic polarity, rational band structure and {001} active facets co-beneficial for robust photooxidation capability. *Journal of Materials Chemistry A* **3**, 24547–24556, doi:10.1039/c5ta07655b (2015).
32. Ganose, A. M., Cuff, M., Butler, K. T., Walsh, A. & Scanlon, D. O. Interplay of orbital and relativistic effects in bismuth oxyhalides: BiOF, BiOCl, BiOBr, and BiOI. *Chem Mater* **28**, 1980–1984, doi:10.1021/acs.chemmater.6b00349 (2016).
33. Li, J., Yu, Y. & Zhang, L. Bismuth oxyhalide nanomaterials: layered structures meet photocatalysis. *Nanoscale* **6**, 8473–8488, doi:10.1039/c4nr02553a (2014).
34. Jiang, J., Zhao, K., Xiao, X. & Zhang, L. Synthesis and facet-dependent photoreactivity of BiOCl single-crystalline nanosheets. *Journal of the American Chemical Society* **134**, 4473–4476, doi:10.1021/ja210484t (2012).
35. Zhu, Y., Yao, W. & Zong, L. *Photocatalysis: application on environmental purification and green energy*. 524 (2014).
36. Pan, Z., Zhang, G. & Wang, X. Polymeric Carbon Nitride/Reduced Graphene Oxide/Fe₂O₃: All-Solid-State Z-Scheme System for Photocatalytic Overall Water Splitting. *Angew Chem Int Ed Engl*, doi:10.1002/anie.201902634 (2019).
37. Wang, Q. *et al.* Artificial photosynthesis of ethanol using type-II g-C₃N₄/ZnTe heterojunction in photoelectrochemical CO₂ reduction system. *Nano Energy* **60**, 827–835, doi:10.1016/j.nanoen.2019.04.037 (2019).
38. Yang, M. Q. *et al.* Self-surface charge exfoliation and electrostatically coordinated 2D hetero-layered hybrids. *Nat Commun* **8**, 14224, doi:10.1038/ncomms14224 (2017).
39. Wang, Q. *et al.* Single Atomically Anchored Cobalt on Carbon Quantum Dots as Efficient Photocatalysts for Visible Light-Promoted Oxidation Reactions. *Chemistry of Materials*, doi:10.1021/acs.chemmater.9b03708 (2020).
40. Yu, H. *et al.* Liquid-phase exfoliation into monolayered BiOBr nanosheets for photocatalytic oxidation and reduction. *ACS Sustainable Chemistry & Engineering* **5**, 10499–10508, doi:10.1021/acssuschemeng.7b02508 (2017).
41. Lang, X., Ji, H., Chen, C., Ma, W. & Zhao, J. Selective formation of imines by aerobic photocatalytic oxidation of amines on TiO₂. *Angew Chem Int Ed Engl* **50**, 3934–3937, doi:10.1002/anie.201007056 (2011).
42. Zhang, N. *et al.* Oxide defect engineering enables to couple solar energy into oxygen activation. *Journal of the American Chemical Society* **138**, 8928–8935, doi:10.1021/jacs.6b04629 (2016).
43. Su, F. *et al.* Aerobic oxidative coupling of amines by carbon nitride photocatalysis with visible light. *Angewandte Chemie International Edition* **50**, 657–660, doi:10.1002/anie.201004365 (2011).

Table

	%	Bi	O	X (Cl\Br\I)
BOH	VB	16.8	83.2	-
	CB	61.4	38.6	-
BOH-Cl	VB	17.0	81.6	1.4
	CB	61.6	37.2	1.1
BOH-Br	VB	16.9	80.7	2.4
	CB	61.4	37.3	1.4
BOH-I	VB	17.1	79.0	3.9
	CB	61.2	37.2	1.6

Table 1| The contributions of Bi, O and X (X = Cl, Br, I) to the near band edges.

Methods

Materials. Bismuth nitrate pentahydrate ($\text{Bi}(\text{NO}_3)_3 \cdot 5\text{H}_2\text{O}$) was obtained from Aladdin. Potassium chloride (KCl), potassium bromide (KBr), potassium iodide (KI), acetonitrile (CH_3CN), anhydrous ethanol were purchased from Sinopharm Chemical Reagent. Benzylamine was bought from TCI. Polyvinylpyrrolidone (PVP, M.W. 8,000) and mannitol were purchased from Alfa Aesar. Biphenyl was purchased from Acros Organics. N-benzylidenebenzylamine was obtained from Sigma-Aldrich. SOD (Superoxide Dismutase, $\geq 1,400$ units/mg dry weight) was acquired from Aladdin. All chemicals were of analytical grade purity.

Characterizations. The crystal phases of BOH and BOH-X (X = I, Br, Cl) were measured using X-ray diffractometer (XRD, Bruker-D8) with Cu K α radiation ($\lambda = 1.5418 \text{ \AA}$). Scanning electron microscopy (SEM, Hitachi-SU8010) and transmission electron microscopy (TEM, Hitachi-7700) were used to obtain the structure and morphology of the samples. High-resolution transmission electron microscope (HRTEM, JEM-2010F) of 200 kV was used to acquire more refined structure of the samples. High-angle annular dark-field scanning TEM (HAADF-STEM) was performed on a high-resolution transmission electron microscope (JEM-ARM200F) operated at 300 kV with a probe spherical aberration corrector. The surface properties were characterized by X-ray photoelectron spectroscopy (XPS, ESCALAB-250XI) with a ULVACPHI Quantera microprobe; the bulk properties were analyzed by X-ray photoelectron spectroscopy (XPS, ULVACPHI-Quantera) with Ar⁺ sputtering. The binding energies were calibrated with respect to the C 1s peak (284.8 eV) from adventitious carbon. UV–visible spectrophotometer (UV-DRS, Hitachi-U3010) was employed to investigate UV–visible diffuse reflectance spectra. The steady photoluminescence spectra were recorded with a fluorescence spectrophotometer (PL, Perkin Elmer-LS55) at room

temperature; the transient photoluminescence spectra were obtained on the Edinburgh FLS920 equipment (excited at 367 nm).

Preparation of BOH nanorods. The BOH NRs were prepared by a facile one-pot hydrothermal method. Specifically, $\text{Bi}(\text{NO}_3)_3 \cdot 5\text{H}_2\text{O}$ (486 mg) was added to deionized water (30 mL), where PVP (400 mg) and mannitol (200 mg) had been added. After stirred for 1 h, the mixture was transferred into a 50 mL Teflon-lined autoclave, and subjected to hydrothermal reaction at 160 °C for 24 h. After cooling, white BOH solid was obtained. The product was washed repeatedly with deionized water and ethanol, and dried in vacuum oven at 60 °C for 8 h.

Preparation of ion-exchanged samples. Typically, BOH (60.8 mg) was dispersed in deionized water (4 mL) via sonication, and a solution (4 mL) of KI (0.1 mmol) was added dropwise. Then, the suspension was sealed into a 12 mL Teflon-lined autoclave, and kept at 60 °C for 12 h. Similarly, the obtained precipitate (BOH-I) was washed repeatedly with deionized water and ethanol, and dried in vacuum oven at 60 °C for 8 h. BOH-Br, BOH-Cl were prepared in the same way except that KI was replaced respectively with KBr or KCl.

Photocatalytic reaction. Typically, the photocatalyst (20 mg) was dispersed in acetonitrile (3 mL) containing benzylamine (0.1 mmol). Then the solution was transferred into a 10 mL quartz tube, with continuous stirring at a proper rotation rate. The photocatalytic reactions were performed with a balloon filled with O_2 (~1 atm). After O_2 bubbling for 30 min, a 300 W Xenon lamp source (Beijing Perfectlight-Microsolar 300) with a 400 nm cutoff filter was switched on. All the reactions progressed at room temperature with an electric fan. The energy output of Xenon lamp was approximately $400\text{mW}\cdot\text{cm}^{-2}$, which was detected by an optical power and energy meter (Thorlabs- PM100D). After irradiation for 6h, the mixture was collected and then separated by centrifugation. To identify the reaction product, gas chromatography-mass spectrometry (GC-MS, Thermo Fisher-ISQ system) with an ECD detector (Thermo Trace GC Ultra) was used. Gas chromatography (GC, Thermo Fisher-Trace 1300) with a FID detector was employed to quantitatively analyze the resultant solution, with 10 mg biphenyl as the internal standard reference.

Active species tests for BOH-I photocatalyst followed the afore-mentioned method, except with extra scavenger agent added. We selected potassium persulfate ($\text{K}_2\text{S}_2\text{O}_8$, 0.1 mmol), triethanolamine (TEOA, 0.1 mmol) and superoxide dismutase (SOD, 1 mg) as scavengers for electron (e^-), hole (h^+) and superoxide radicals ($\times\text{O}_2^-$), respectively.

Conversion of benzylamine and selectivity for *N*-benzylbenzaldimine are defined in the follow equations:

Conversion (%)

$$= \frac{\sum \text{content (mmol) of each product analyzed via GC}}{\text{benzylamine (mmol)}} \times 100\%$$

$$\text{Selectivity (\%)} = \frac{N\text{-benzylbenzaldimine (mmol)}}{\sum \text{content (mmol) of each product}} \times 100\%$$

EPR test. To capture the signal of $\cdot\text{O}_2^-$ radicals, electron paramagnetic resonance spectra were recorded on an electron paramagnetic resonance spectrometer (EPR, JEOL FA-200). Typically, the catalyst sample (5 mg) and benzylamine (0.2 mmol) were dispersed in acetonitrile (1 mL) with 10 μL 5, 5-dimethyl-1-pyrroline *N*-oxide (DMPO). The mixture was transferred into a paramagnetic tube. Upon irradiation with 300 W Xe lamp ($\lambda > 420$ nm), the ESR spectra were recorded.

Electrochemical measurements. The catalyst (5 mg) was dispersed in deionized water (1 mL). The mixture was deposited dropwisely on the pretreated indium tin oxide (ITO) wafer and then dried for 24 h at ambient temperature. The Mott–Schottky experiments were conducted to evaluate the band positions of BOH and BOH-X. Measurements were performed on an electrochemical workstation (PMC-500, Princeton) with a standard three-electrode system. The catalyst was used as the working electrode, while a Pt foil and Ag/AgCl electrode served as the counter electrode and the reference electrode, respectively. All the experiments employed an aqueous Na_2SO_4 solution ($0.1 \text{ mol}\cdot\text{L}^{-1}$) as the electrolyte, and were conducted within the potential range from -0.7 to -0.1 V at a frequency of 500 Hz.

Theoretical calculations. Theoretical calculations were performed using Vienna ab initio simulation packages (VASP) based on density functional theory¹. Interactions between core and valence electrons were described by the projector augmented wave (PAW) pseudopotentials². The generalized gradient approximation (GGA) in the scheme of proposed by Perdew, Burke, and Ernzerhof (PBE) was adopted to express the electron exchange correlation with a cutoff energy of 400 eV, while the van der Waals effect and hydrogen bonding interactions were accounted for by the DFT-D3³. All atoms were fully relaxed in 3 dimensions till all residual forces have declined below $0.02 \text{ eV}\ \text{\AA}^{-1}$ and the convergence of energy were set to 1×10^{-5} eV. The Brillouin zone was sampled by the Monkhorst–Pack method with a $2 \times 1 \times 1$ k-point grid⁴.

References

1. Kresse, G.; Furthmüller, J. Efficient iterative schemes for ab initio total-energy calculations using a plane-wave basis set. *Phys. Rev. B: Condens. Matter Mater. Phys.* 1996, 54, 11169-11186.
2. Blochl, P. E. Projector augmented-wave method. *Phys. Rev. B: Condens. Matter Mater. Phys.* 1994, 50, 17953-17979.
3. Perdew, J. P.; Burke, K.; Ernzerhof, M. Generalized gradient approximation made simple. *Phys. Rev. Lett.* 1996, 77, 3865-3868.
4. Monkhorst, H. J.; Pack, J. D. Special points for Brillouin-zone integrations. *Phys. Rev. B: Condens. Matter Mater. Phys.* 1976, 13, 5188-5192.

Scheme

Scheme 1 is available in the Supplementary Files

Figures

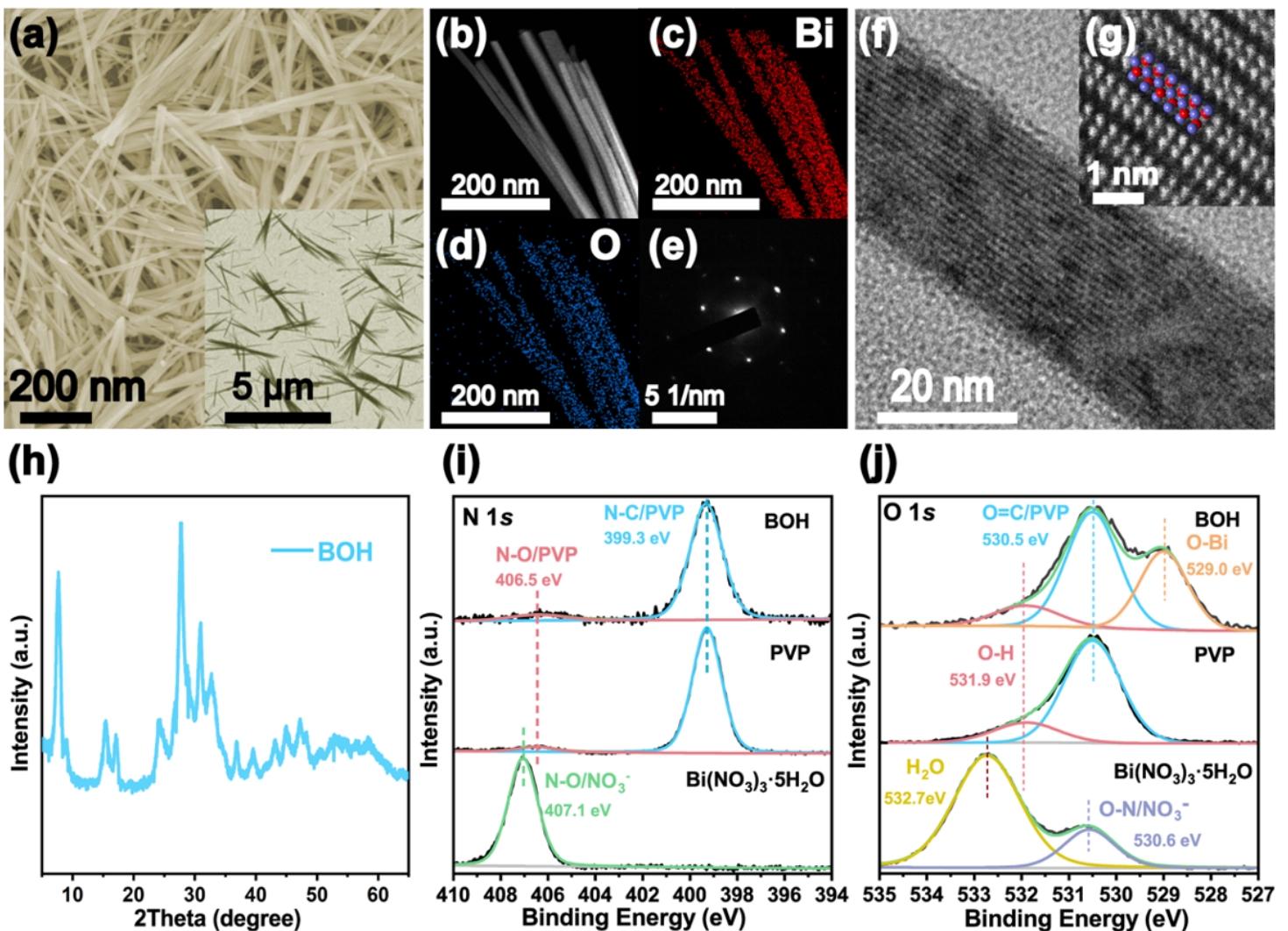


Figure 1

Structure characterizations of BOH. (a) SEM image; inset, TEM image; (b) HAADF-STEM image; (c, d) EDS mapping for Bi and O, respectively; (e) SAED pattern; (f) HRTEM image; (g) atomic-resolution AC HAADF-STEM image; the overlaying model image showing the structure of $[\text{Bi}_2\text{O}_2]^{2+}$ layer in $\text{Bi}_2\text{O}_2(\text{OH})(\text{NO}_3)$ (red balls, Bi atoms; blue balls, O atoms); (h) XRD pattern; (i, j) XPS spectra for N, O in BOH, PVP and $\text{Bi}(\text{NO}_3)_3 \cdot 5\text{H}_2\text{O}$, respectively.

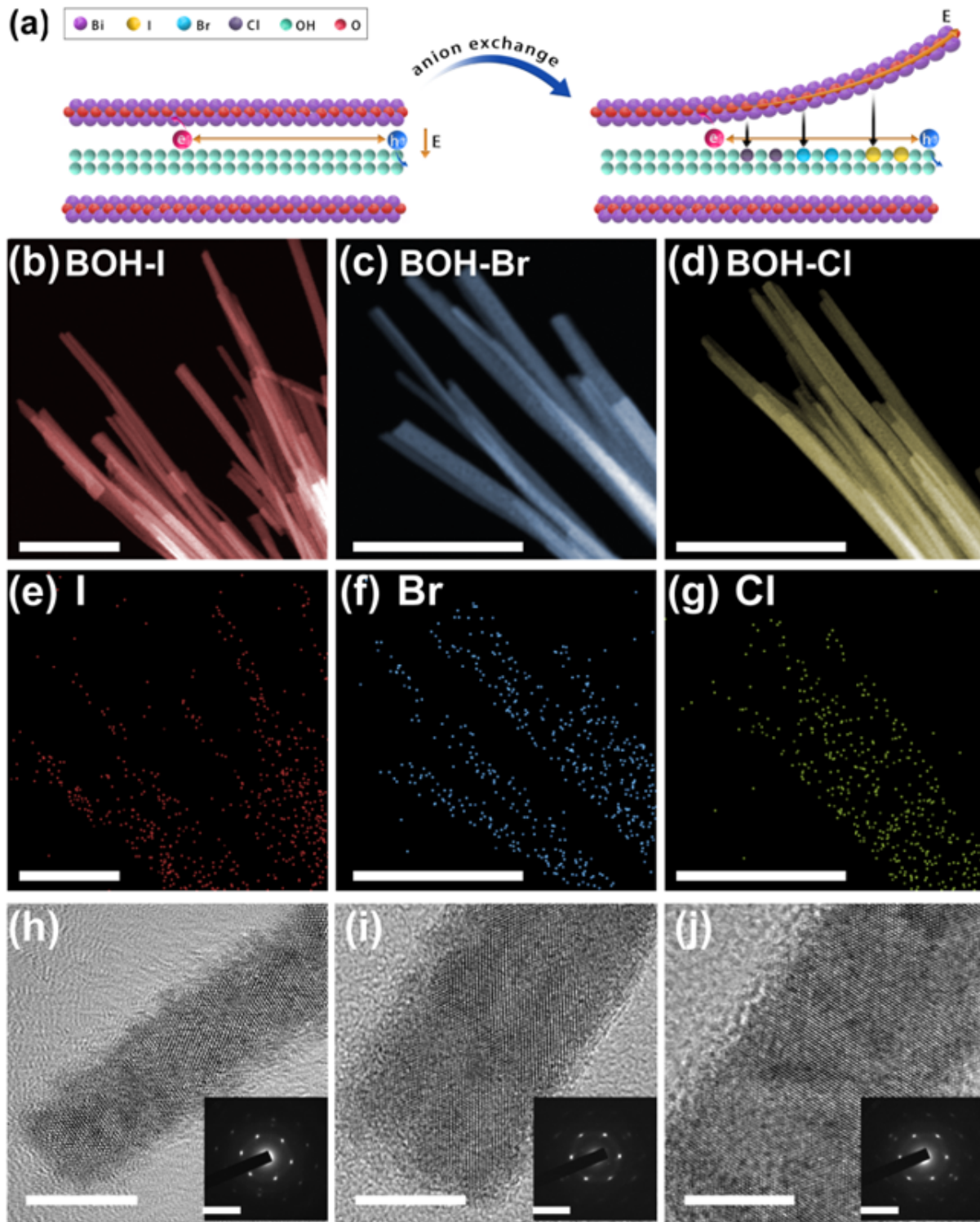


Figure 2

Structural characterizations of the BOH-X products obtained via anion exchange. (a) Schematic illustration of the halide-anion exchange process; (b–d) dark-field HRTEM images (scale bar, 200 nm); (e–g) EDS mapping of halogen atoms (scale bar, 200 nm); (h–j) HRTEM-STEM images (scale bar, 10 nm); insets: SAED patterns (scale bar 0.2 nm^{-1}).

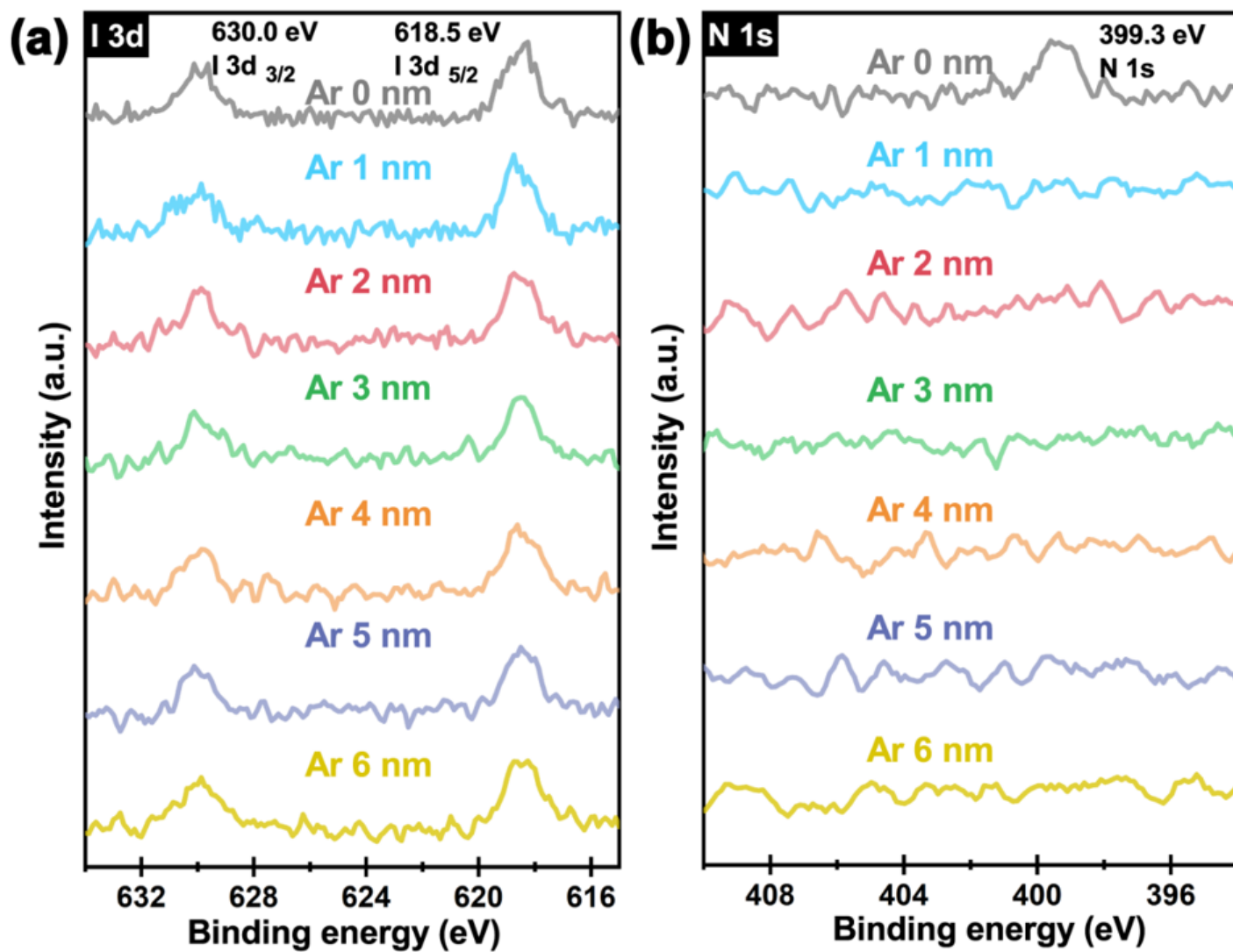


Figure 3

High-resolution XPS spectra with Ar⁺ sputtering at different depths. (a) I 3d and (b) N 1s for BOH-I.

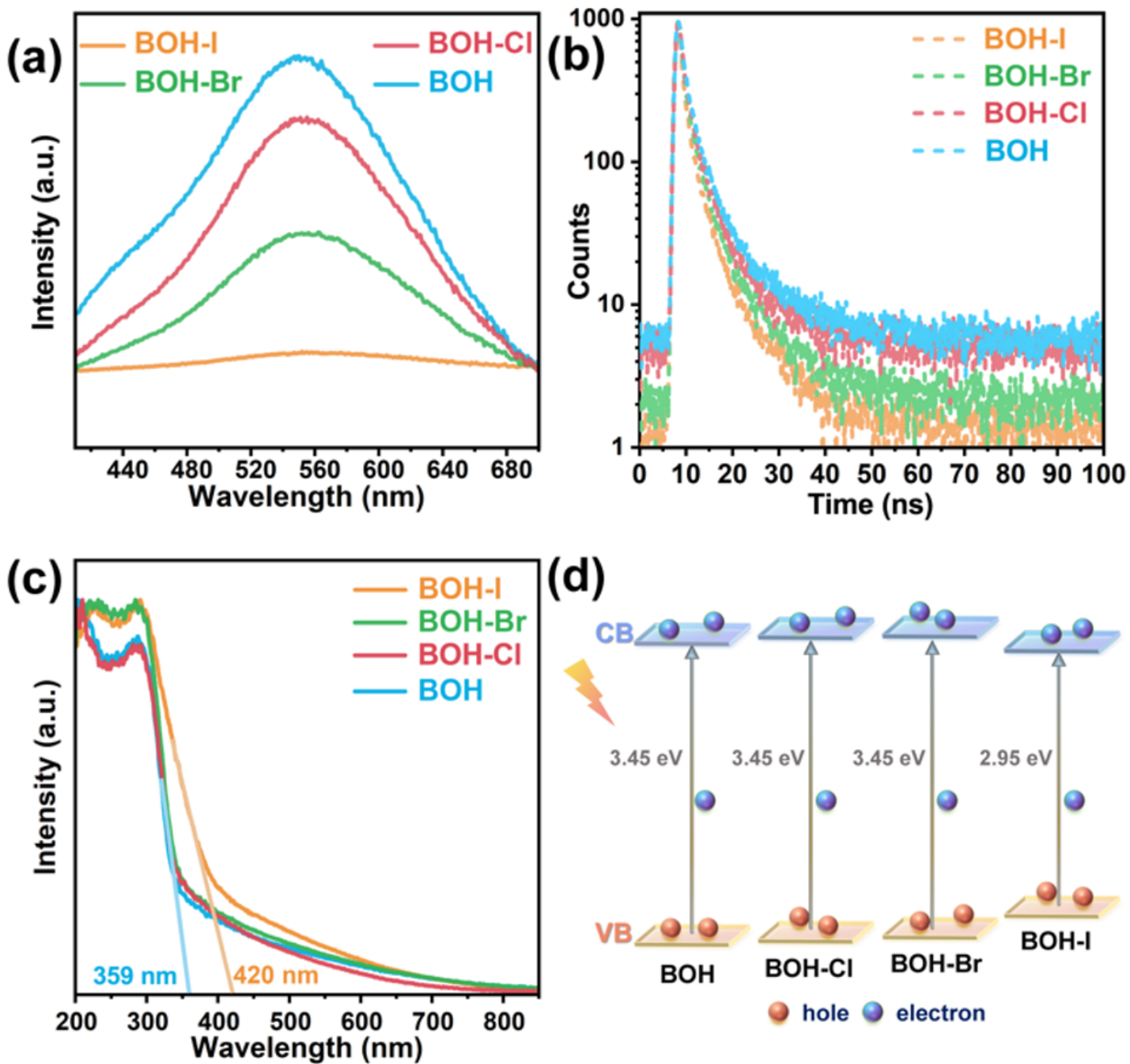


Figure 4

Spectroscopic characterizations on BOH and BOH-X samples. (a) steady Photoluminescence spectra (excitation wavelength, 346 nm); (b) transient Photoluminescence spectra (excitation wavelength, 367 nm); (c) UV-vis diffuse reflectance spectra; (d) diagrams of the band structures for the four samples.

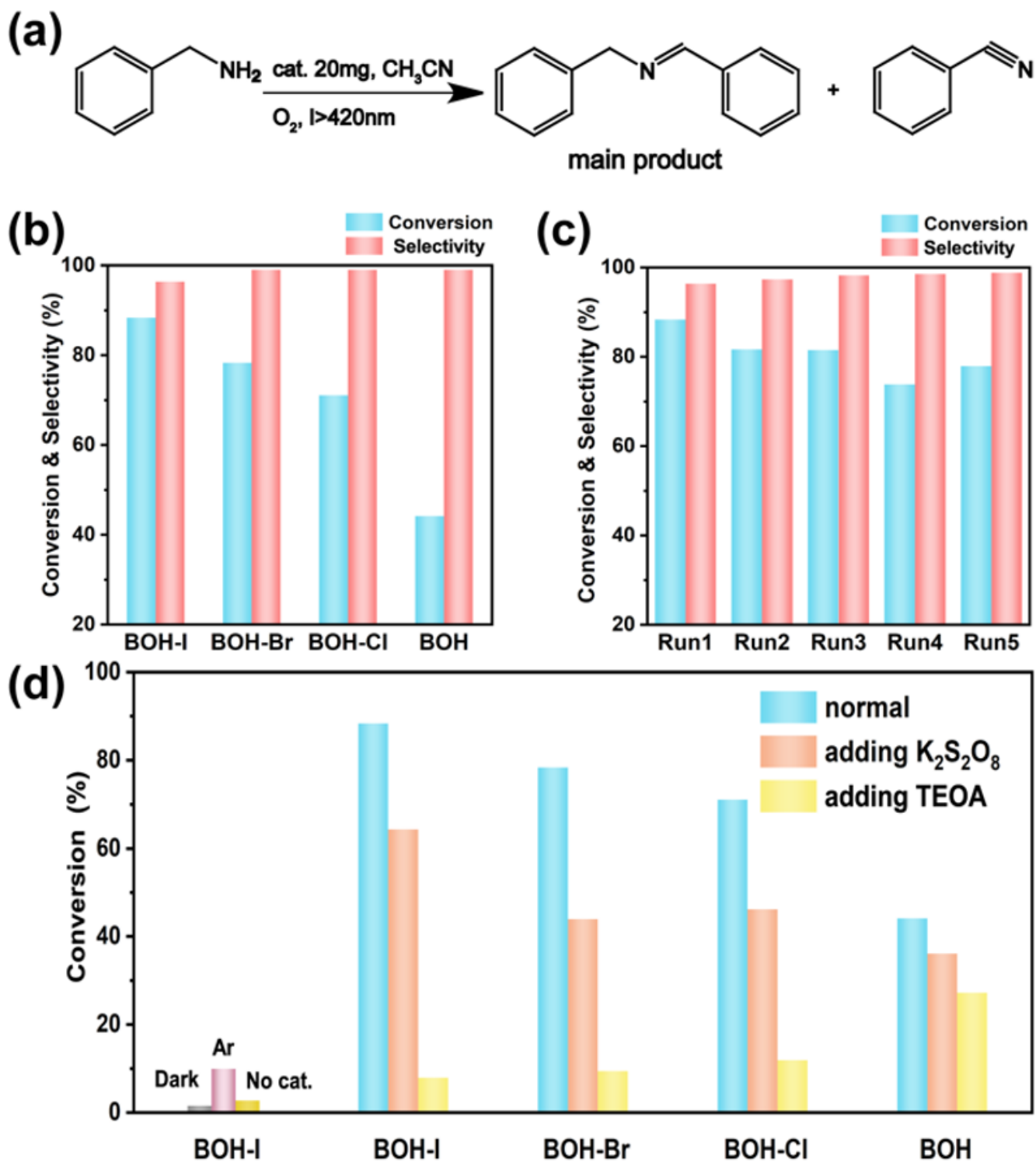


Figure 5

Photocatalytic activity. (a) Equation of photocatalytic oxidative coupling of benzylamine; (b) catalytic performances over BOH and BOH-X samples; (c) results of recycle experiment on BOH-I; (d) catalytic performances over BOH and BOH-X under normal conditions and with different scavenging agent, and the catalytic performances over BOH-I in dark or under Ar atmosphere.

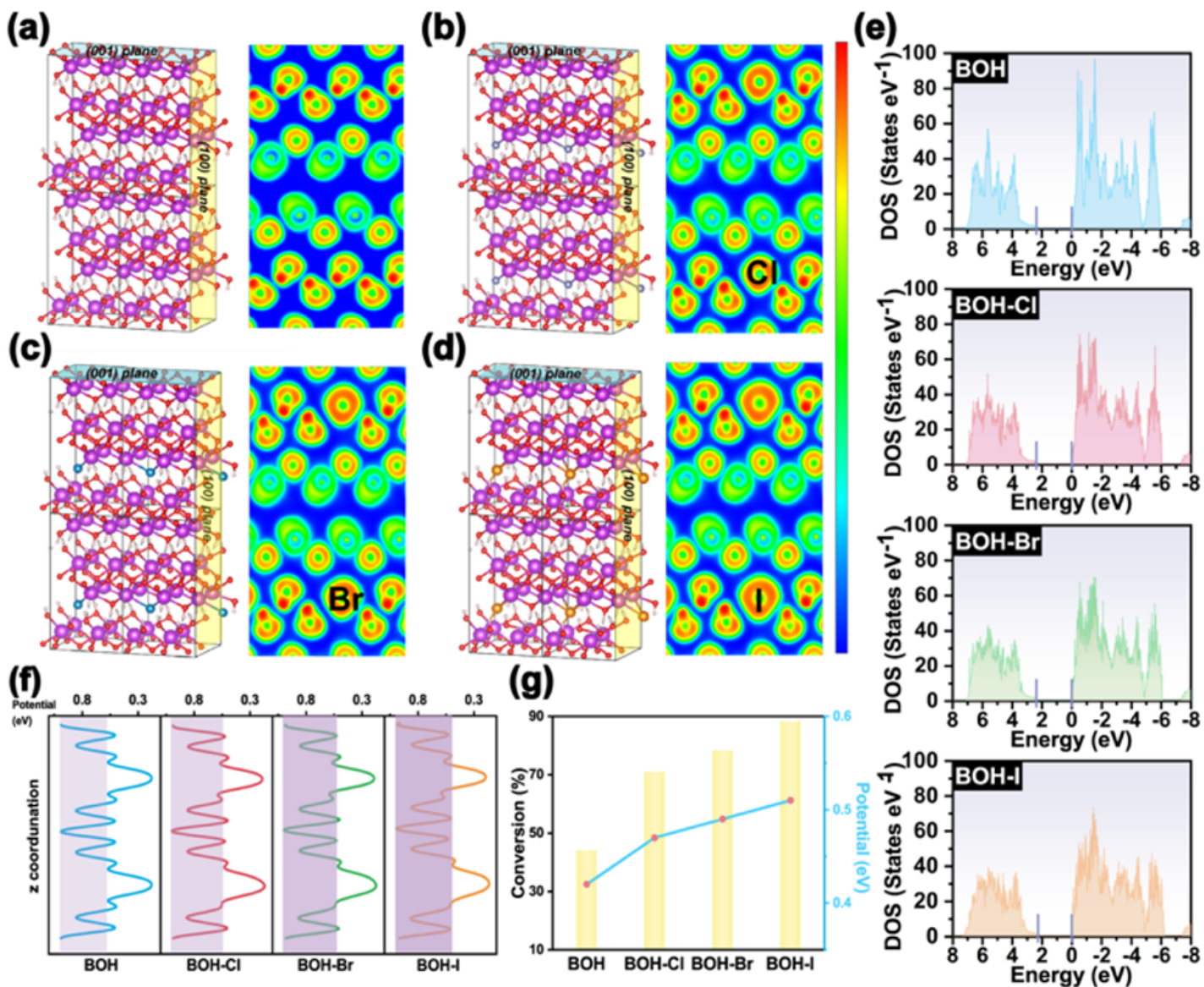


Figure 6

Theoretical calculation. (a–d) Crystallographic structures and charge distributions for BOH, BOH-Cl, BOH-Br and BOH-I, respectively (The isosurface value is 0.005 e Bohr⁻³.); (e) Calculated DOS for the four catalysts; (f) DFT calculated local internal electric field for the four catalysts (The purple shaded parts represents the interlamellar IEF); (g) superimposed plots of benzylamine conversion and IEF intensity for the four catalysts.

Supplementary Files

This is a list of supplementary files associated with this preprint. Click to download.

- [Scheme1.png](#)
- [SI.docx](#)